

Article

Mineralogical and Geochemical Constraints on the Occurrence Forms of REEs in Carboniferous Karst Bauxite, Central Guizhou Province, Southwest China: A Case Study of Lindai Bauxite

Chaokun Luo ^{1,2}, Peng Liang ³, Ruidong Yang ^{1,2,*}, Junbo Gao ^{1,2} , Qun Chen ³ and Hongcheng Mo ^{1,2}¹ College of Resources and Environmental Engineering, Guizhou University, Guiyang 550025, China² Key Laboratory of Karst Georesources and Environment, Ministry of Education, Guizhou University, Guiyang 550025, China³ 115 Geological Party, Guizhou Bureau of Geology & Mineral Exploration, Qingzhen 551400, China

* Correspondence: rdyang@gzu.edu.cn

Abstract: Karst bauxite is a major source of aluminum and contains high concentrations of trace elements such as Li, Ga, Sc, and rare earth elements (REEs). It is regarded as a potential non-conventional REE source due to the increasing demand for REEs. This study provides new mineralogical and geochemical evidence of a Lindai bauxite deposit in central Guizhou Province, aiming to analyze the genesis of REE minerals and reveal the forms of REEs occurring in these deposits. The results indicate that a large number of detrital and authigenic rare-earth phosphate minerals, including monazite and xenotime, were identified. In terms of their genesis, the authigenic monazite was mainly precipitated under alkaline and reducing conditions, whereas the authigenic xenotime was formed in acidic and reducing conditions. The mineralogical evidence detected by scanning electron microscopy with energy dispersive spectrometry (SEM-EDS) and a TESCAN Integrated Mineral Analyzer (TIMA) suggests that the REEs in the Lindai bauxite exhibit multiple forms, including rare-earth phosphate minerals (monazite and xenotime) and REE scavenging by hematite and anatase phases. Among them, the anatase controls some LREE (such as La, Ce, and Pr) distributions in addition to monazite, whereas the hematite also controls relatively large amounts of Sm, Eu, and HREE (such as Gd, Tb, Dy, Ho, Er, Tm, and Lu) distributions. According to the calculation of the percentage of REE-bearing mineral phases obtained by a TIMA analysis, REE scavenging by hematite accounted for 93.28% of all forms of REEs, REE scavenging by anatase accounted for 5.88%, monazite accounted for 0.67%, and xenotime accounted for 0.17%. This study provides new evidence of the forms of REEs occurring in Carboniferous karst bauxite in central Guizhou Province.

Keywords: REE minerals; monazite; xenotime; REE scavenging; karst bauxite

Citation: Luo, C.; Liang, P.; Yang, R.; Gao, J.; Chen, Q.; Mo, H. Mineralogical and Geochemical Constraints on the Occurrence Forms of REEs in Carboniferous Karst Bauxite, Central Guizhou Province, Southwest China: A Case Study of Lindai Bauxite. *Minerals* **2023**, *13*, 320. <https://doi.org/10.3390/min13030320>

Academic Editors: Ali Abedini and Maryam Khosravi

Received: 5 February 2023

Revised: 20 February 2023

Accepted: 22 February 2023

Published: 24 February 2023



Copyright: © 2023 by the authors. Licensee MDPI, Basel, Switzerland. This article is an open access article distributed under the terms and conditions of the Creative Commons Attribution (CC BY) license (<https://creativecommons.org/licenses/by/4.0/>).

1. Introduction

Rare earth elements (REEs) are defined as critical raw materials by the European Union [1]. They are crucial elements used in the green energy, defense, aerospace, medical, automotive, and electronic industries [2,3]. The most well-known and economically important REE deposits include carbonatite, alkaline igneous, peralkaline igneous, ion adsorption, laterite, and hydrothermal types [4]. Karst bauxite, the main source of aluminum, also contains high concentrations of trace elements such as Li, Ga, Sc, and REEs [5–13]. Many scholars in recent years have regarded karst bauxite and red mud generated by alumina production using the Bayer process as a potential non-conventional REE resource due to the increasing demand for REEs [3].

As a crucial bauxite resource in China, karst bauxites are mainly located in the Shanxi, Henan, Guangxi, Guizhou, and Yunnan Provinces and Chongqing city [14]. They were formed during the Carboniferous and Permian periods. It is generally accepted that the forms of REEs in the bauxite of China occur via (1) adsorption on clay and other mineral

surfaces in the form of ions and (2) isomorphous substitution in some minerals [15]. In contrast, foreign scholars commonly believe that the enrichment of REEs in bauxite is due to the crystallization of authigenic REE minerals, accumulation of detrital phases, and ionic adsorption on the surface of the clay and other minerals [16–18]. However, since REE minerals, including parisite and churchite, were first reported in the Quyang karst bauxite of the Guangxi Province [15], more REE minerals were identified in numerous karst bauxite deposits, including synchysite, bastnäsite, cerianite, and churchite in the Wulong-Nanchuan bauxite of Chongqing city [19]; parisite in the bauxite of northern Guizhou Province [20]; bastnäsite, parisite, cerianite, rhabdophane, and churchite in the bauxite of western Guangxi Province [5]; and xenotime in the bauxite of western Henan Province [21].

The bauxites in Guizhou Province mainly occur in the Lower Carboniferous Jiujiayu Formation in central Guizhou and the Lower Permian Dazhuyuan Formation in northern Guizhou. More than 90 deposits (mining sites) have been found in central Guizhou, and the total resource reserves are estimated at 518 million tons [22]. Although numerous studies have investigated the mineralogy, geochemistry, parental affinity, and metallogenic patterns in the past two decades [9,23–28], the forms of REEs have yet to be identified. Particularly, this study has important implications for further exploration and utilization of REEs occurring in karst bauxite. Numerous studies have indicated that the karst bauxites in central Guizhou also contains relatively high REE concentrations. For instance, Long et al. [9] reported Σ REE contents in the Yunfeng bauxite ores of 266.3 ppm to 2188 ppm (mean 1051 ppm). Wu et al. [29] reported Σ REE contents of 208.9 ppm to 772.0 ppm (mean 403.6 ppm) in the Maochang bauxite ores. Luo et al. [28] reported Σ REE contents in the Lindai bauxite ores of 734.7 ppm to 1756 ppm (mean 1350 ppm). Based on these considerations, this study focuses on the most representative Lindai bauxite deposit in central Guizhou Province. The primary objectives of our study are to analyze the genesis of REE minerals and reveal the forms of REEs occurring in these deposits.

2. Geological Setting

2.1. Regional Geology

Geotectonically, central Guizhou is positioned on the southwestern border of the Yangtze Craton of the South China Block (Figure 1a). This area has been a stable passive continental margin since the late Sinian period, forming a set of thick sedimentary formations dominated by marine carbonate rock intercalated with fine detrital rock during the Cambrian period [30]. At the end of the Ordovician period, the Caledonian Movement resulted in the exposure of Cambrian and Ordovician stratigraphic units in central Guizhou, forming the Qianzhong Uplift [31]. Subsequently, after nearly 100 million years of large-scale weathering and erosion, central Guizhou became a karstic plain at the end of the Devonian period [23]. Central Guizhou had karstic depressions and lakes during the Carboniferous Visean age due to the large-scale transgression of the South China Sea from south to north [23]. During this time, the primary bauxitic materials weathered from the underlying bedrock were transported into these karst landforms, depositing a set of ore-bearing rock series in the Lower Carboniferous Jiujiayu Formation [28].

The regional structure is relatively complex, dominated by NE-trending folds, as well as NE-, NNE-, and NW-trending faults (Figure 1b). The Paleozoic sedimentary records from oldest to youngest comprise the Cambrian Niutitang Formation, Mingxinsi Formation, Jindingshan Formation, Qingxudong Formation, Gaotai Formation, Shilengshui Formation, Loushanguan Formation, Carboniferous Jiujiayu Formation, Baizuo Formation, Permian Liangshan Formation, Qixia Formation, Maokou Formation, Longtan Formation, Changxing Formation, and Dalong Formation (Figure 2). The Carboniferous karst bauxite deposits in central Guizhou are hosted in the Lower Carboniferous Jiujiayu Formation, which overlies the paleokarst weathered surface of the Cambrian carbonate rock and underlies the Lower Carboniferous Baizuo Formation dolomite. According to the sequence stratigraphy, palaeopalynology, and palaeobotany, the Jiujiayu Formation was formed in the early middle stage of the Mississippian Visean age [32–34].

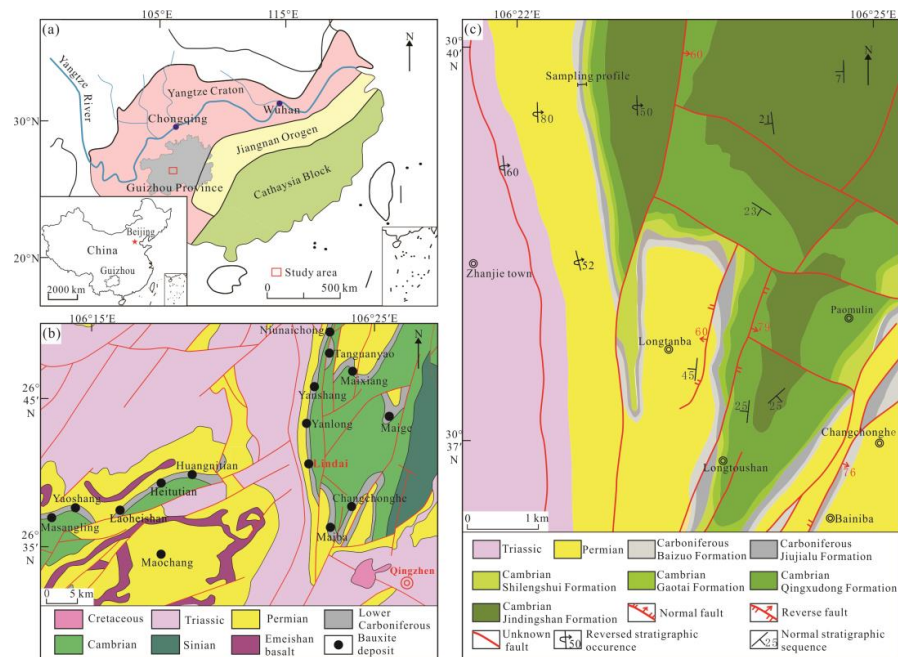


Figure 1. (a) Map of the South China Block showing the location of the study area in the Yangtze Craton. (b) Regional geological map of the Qingzhen bauxite ore field. (c) Geological map of the Lindai bauxite showing the sampling location.

Age (Ma)	System	Series	Qingzhen-Xiuiwen area	Guiyang area	Lithologic features	Tectonic movement
259.1	Permian	Lopingian	Dalong Formation		Predominately by the procelanite intercalated with clay stone	Dongwu Movement
			Changxing Formation		Predominately by the flint-nodule-containing limestone intercalated with clay stone	
		Guadalupian	Longtan Formation		Predominately by the siltstone, shale and clay stone intercalated with coal seam	
			Maokou Formation		Predominately by the limestone	
			Qixia Formation		Predominately by the flint-nodule-containing limestone	
272.0		Cisuralian	Liangshan Formation		Predominately by the quartz sandstone, shale and carbonaceous shale	
298.9	Carboniferous	Mississippian/Devonian	Gzhelian			Ziyun Movement
			Kasimovian			
			Moscovian			
			Bashkirian			
			Serpukhovian	Baizuo Formation		
323.2		Viscan	Jiujialu Formation		Predominately by the ferruginous rock, bauxitic rock, bauxite layer and clay stone	
358.9		Tournaisian				
382.7	Devonian	Upper		Gaopochang Formation	Predominately by the dolomite	
				Mangshan Group	Predominately by the quartz sandstone	
393.3	Devonian	Middle				
419.2	Silurian	Lower				Caledonian Movement
423.4	Silurian	Ludlow				
433.4	Silurian	Wenlock				
443.8	Silurian	Llandovery		Gaozhaitian Formation	Predominately by the sandstone and shale	
458.4	Ordovician	Upper		Huanghuachong Formation	Predominately by the limestone	
470	Ordovician	Middle		Meitan Formation	Predominately by the shale, arenaceous shale intercalated with sandstone	
				Honghuayuan Formation	Predominately by the bioclastic limestone and limestone	
				Tongzi Formation	Predominately by the dolomite intercalated with shale	
485.4	Ordovician	Lower				Yunan Movement
497	Cambrian	Furongian		Loushanguan Group	Predominately by the dolomite	
509	Cambrian	Miaolingian		Shilengshui Formation	Predominately by the dolomite, argillaceous dolomite and clay stone	
				Gaotai Formation	Predominately by the argillaceous dolomite, dolomitic mudstone and shale	
				Qingxudong Formation	Predominately by the dolomite, argillaceous dolomite, marlstone and calcareous shale	
	Cambrian	Series 2		Jindingshan Formation	Predominately by the sandstone and shale	
				Mingxinsi Formation	Predominately by the mudstone, shale and sandstone	
				Niutitang Formation	Predominately by the mudstone and shale	

Figure 2. Paleozoic stratigraphic sequences in central Guizhou area (modified from [28]).

2.2. Deposit Geology

The Lindai bauxite deposit is located 25 km northwest of Qingzhen city in central Guizhou. The stratigraphic units from oldest to youngest include the Cambrian carbonate rock and fine detrital rock (i.e., Jindingshan Formation, Qingxudong Formation, Gaotai Formation, and Shilengshui Formation), Carboniferous ore-bearing rock series (i.e., Jiujialu Formation) and dolomite (i.e., Baizuo Formation), Permian fine detrital rock and carbonate rock (i.e., Liangshan Formation, Qixia Formation, Maokou Formation, Longtan Formation, Changxing Formation, and Dalong Formation), and Triassic dolomite (Figures 1c and 2). The Jiujialu Formation ore-bearing rock series unconformably overlies the Shilengshui Formation and underlies the Baizuo Formation (Figure 3b). The Shilengshui Formation

consists of dolomite intercalated with hydromica claystone and purple-red mudstone, representing the autochthonous basement of the Jiujialu Formation. The Baizuo Formation consists of dolomite and dolomitic limestone, representing the cover rock of the Jiujialu Formation. The thickness of the Jiujialu Formation varies from several meters to more than twenty meters and contains three layers based on the following lithologic characteristics from bottom to top [27]: (1) the lower layer is 0 to 8 m thick, consisting of iron-rich bauxitic claystone and bauxitic claystone, (2) the middle layer is 0 to 10 m thick, consisting of stratiform and lenticular bauxite orebodies, and (3) the upper layer is 0 to 6 m thick, consisting of bauxitic claystone, carbonaceous shale with abundant pyrite nodules, and fossil plant fragments (Figure 3a). The bauxite ore is grey and is represented by clastic, pisolitic, and compact structures (Figure 4a–c). Geochemical data suggest that the Lindai bauxite deposit was mainly derived from a mixed lithology, including underlying Cambrian Shilengshui Formation dolomite, hydromica claystone, and purple-red mudstone, rather than single dolomite considered by previous studies [28]. The genesis of the Lindai bauxite deposit, including the parental affinity, mineral genesis, migration and sedimentation, and ore-forming process of the bauxite, has been described in detail by Luo et al. [28].

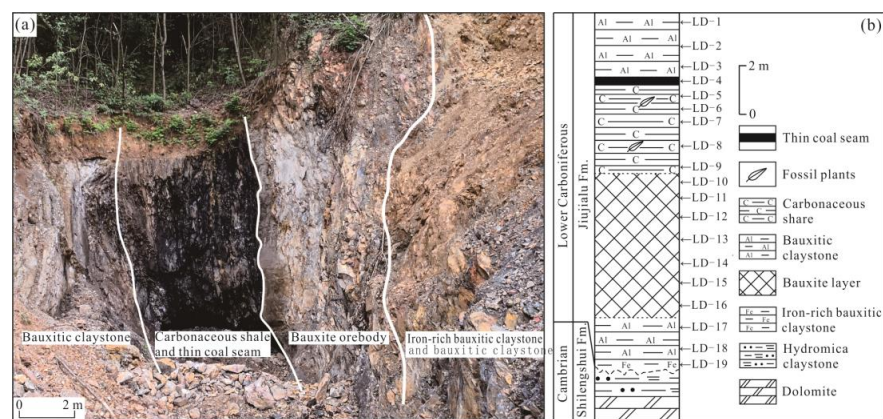


Figure 3. Field photograph and lithostratigraphic column of the Lindai bauxite deposit (modified from [28]). (a) The photograph shows the outcrop of the Lower Carboniferous Jiujialu Formation ore-bearing rock series. (b) Lithostratigraphic column and sampling location of the Lindai bauxite.

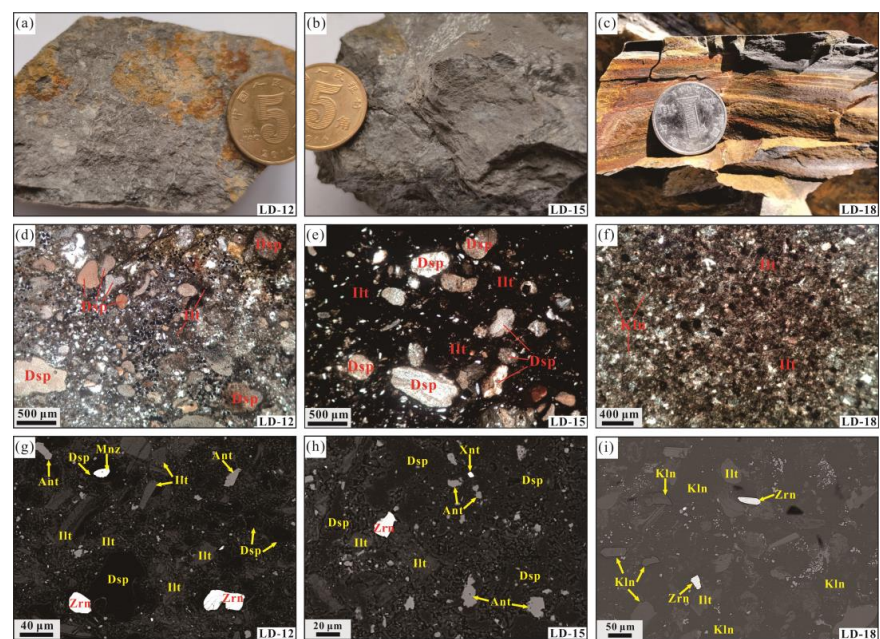


Figure 4. Hand-specimen, microscopical, and SEM backscattered electron (BSE) photographs of the representative bauxite ore and bauxitic claystone samples of the Lindai bauxite deposit. (a) Gray clastic

bauxite ore of the LD-12 sample (modified from [28]). (b) Gray compact bauxite ore of the LD-15 sample. (c) Gray black laminated bauxitic claystone of the LD-18 sample (modified from [28]). (d) Matrix-supported clastic texture in the LD-12 sample (plane-polarized light). (e) Matrix-supported pisolitic texture in the LD-15 sample (plane-polarized light). (f) Pelitomorphic texture in the LD-18 sample (cross-polarized light). (g) Diaspore, illite, anatase, zircon, and monazite in the LD-12 sample. (h) Diaspore, illite, anatase, zircon, and xenotime in the LD-15 sample. (i) Granular kaolinite, illite, and zircon are scattered in the kaolinic matrix in the LD-18 sample. Abbreviations: Dsp = diaspore, Illt = illite, Ant = anatase, Zrn = zircon, Kln = kaolinite, Mnz = monazite, Xnt = xenotime.

3. Sampling and Analytical Methods

A total of 19 samples were selected from the representative vertical profile in the Lindai bauxite deposit, including an upper bauxitic claystone (LD-01–LD-03) and carbonaceous shale (LD-04–LD-09) layer, a middle bauxite ore layer (LD-10–LD-16), and a lower bauxitic claystone (LD-17–LD-18) and ferruginous claystone (LD-19) layer (Figure 3b). The analytical methods, procedures, detection limits, and results of the whole-rock major, trace, and REE contents of all 19 samples have been described in detail by Luo et al. [28]. Here, we further investigate the mineralogical and geochemical characteristics of these representative bauxite ore samples to reveal the forms of REEs occurring in the samples.

The petrography and mineralogy of the bauxite ore samples were obtained by optical microscopy and scanning electron microscopy with energy dispersive spectrometry (SEM-EDS). The micromorphological observations and microchemical determinations of the minerals (including REE minerals) were performed using a JSM-7800F thermal field emission scanning electron microscope (FE-SEM, Japan Electronics Co., Ltd., Tachikawa, Japan) equipped with an TEAM Apollo XL energy dispersive spectrometer (EDS, Britain EDAX Co., Ltd., Cambridge, UK), with the following operating conditions: accelerating voltage of 20 kV, current of 10 nA, working distance of 10 mm, and a beam diameter of 1 μm . Before performing SEM-EDS, a thin section was sprayed with a thin layer of carbon. SEM-EDS was carried out at the State Key Laboratory of Ore Deposit Geochemistry, Institute of Geochemistry, Chinese Academy of Sciences. The petrographical observations were conducted using an Axio Scope A1 (ZEISS) microscope at the College of Resources and Environmental Engineering, Guizhou University.

Mineral and REE scanning maps of the representative bauxite ore samples were obtained by a TESCAN Integrated Mineral Analyzer (TIMA) system at the Nanjing Hongchuang Geological Exploration Technology Service Company. The TIMA consists of a Mira-3 scanning electron microscope with four energy dispersive X-ray spectrometers (EDAX Element 30). The operating conditions were set as: accelerating voltage of 25 kV, probe current of 9 nA, working distance of 15 mm, pixel spacing of 2.5 μm , and dot spacing of 7.5 μm . Before performing TIMA, a thin section was sprayed with a thin layer of carbon. The current and BSE signal strength were calibrated using the automated procedure on the platinum Faraday cup, and the EDS signal was calibrated using the Mn standard sample. The BSE images and EDS data of analytical sample were obtained using TIMA liberation analysis mode. The obtained EDS data were matched with the mineral definition library to identify the mineral and perform mineral mapping.

4. Results and Discussion

4.1. Mineralogy and Petrography

The petrographic study demonstrates that the bauxite ores have primarily a clastic texture, followed by a pisolitic texture (Figure 4d–e), whereas the bauxitic claystone exhibits a pelitomorphic texture (Figure 4f). Notably, the vast majority of clastic textures are matrix-supported, and grain-supported textures only occur locally. In the clastic textures, the grains typically have fine clastic, pseudo-breccia, and occasionally oolitic textures. Grains of various sizes and shapes occur without any sorting or directional structures. They are scattered in the matrices composed of diaspore and clay minerals, indicating that

these bauxite ores have undergone short-distance transportation by gravity flow before sedimentation and were not autochthonous [23,35].

The mineralogical compositions detected by TIMA analysis show that the representative bauxite ore is composed mostly of diaspore (59.65%) and illite (38.06%), followed by minor amounts of anatase (1.11%), kaolinite (0.9%), zircon (0.08%), dravite (0.07%), hematite (0.07%), chamosite (0.03%), monazite (0.008%), and xenotime (0.002%) (Figure 5). Some other minerals were also detected by SEM-EDS, including pyrite, cassiterite, barite, chalcopyrite, galena, arsenopyrite, and REE minerals, such as monazite and xenotime (Figure 4g–i) [28].

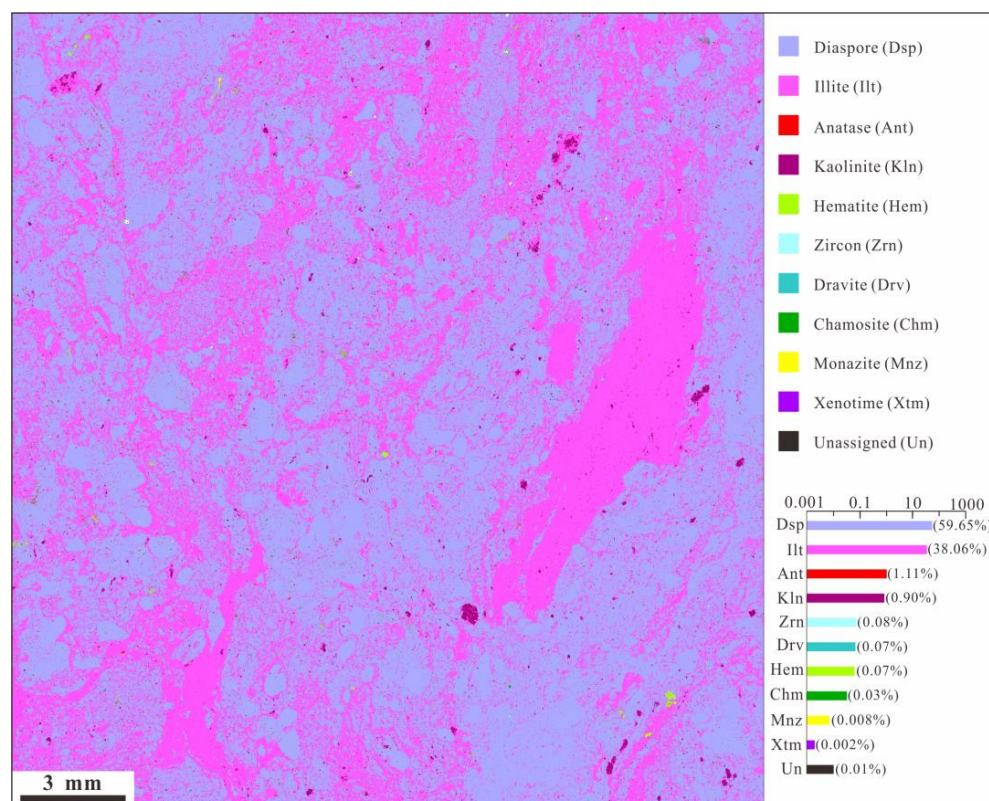


Figure 5. TIMA mineral scanning maps of the representative Lindai bauxite ore. The bar graph on the right side shows the percentage composition of mineral phases in a thin section.

4.2. Geochemical Compositions

A trace element analysis shows that the Jiujiayu Formation ore-bearing rock series contains enriched REE contents. The Σ REE values in the bauxite ore, carbonaceous shale, and bauxitic claystone samples range from 734.7 to 1756 ppm (mean 1350 ppm), 1081 to 2190 ppm (mean 1459 ppm), and 329.7 to 792.9 ppm (mean 547.3 ppm), respectively (Table S1 and Figure 6). Regarding the REE composition, the Ce content is the highest in the bauxite ores, followed by the La, Nd, Pr, Sm, Gd, Dy, Er, and Yb contents (Figure 6). The high Σ light REEs (LREEs, La–Eu)/ Σ heavy REEs (HREEs, Gd–Lu) ratios of the bauxite ore (5.09–12.12), carbonaceous shale (11.12–39.03), and bauxitic claystone (7.58–15.89) samples indicate that the LREEs are significantly enriched relative to the HREEs in all samples. In addition, the Y contents in the bauxite ore, carbonaceous shale, and bauxitic claystone samples range from 109.5 to 304.0 ppm (mean 167.9 ppm), 62.40 to 155.0 (mean 99.52 ppm), and 47.80 to 89.20 (mean 64.04 ppm), respectively.

A correlation analysis (with a significance level of $p < 0.05$) (Figure 7) reveals that the Σ REEs and Σ LREEs have strong negative correlations (correlation coefficient of -0.68 to -0.76) with the Zr and Hf contents. The Σ REEs and Σ LREEs have high positive correlations (correlation coefficient of 0.77 to 0.81) with Na_2O and weak or no correlations

with Al_2O_3 , TiO_2 , SiO_2 , Fe_2O_3 , Nb, and Ta. Conversely, the ΣHREEs have significantly positive correlations (correlation coefficient of 0.81 to 0.96) with P_2O_5 , Fe_2O_3 , Th, and Y. The Th and Y contents have very strong positive correlations (correlation coefficient of 0.79 to 0.87) with the P_2O_5 and Fe_2O_3 contents.

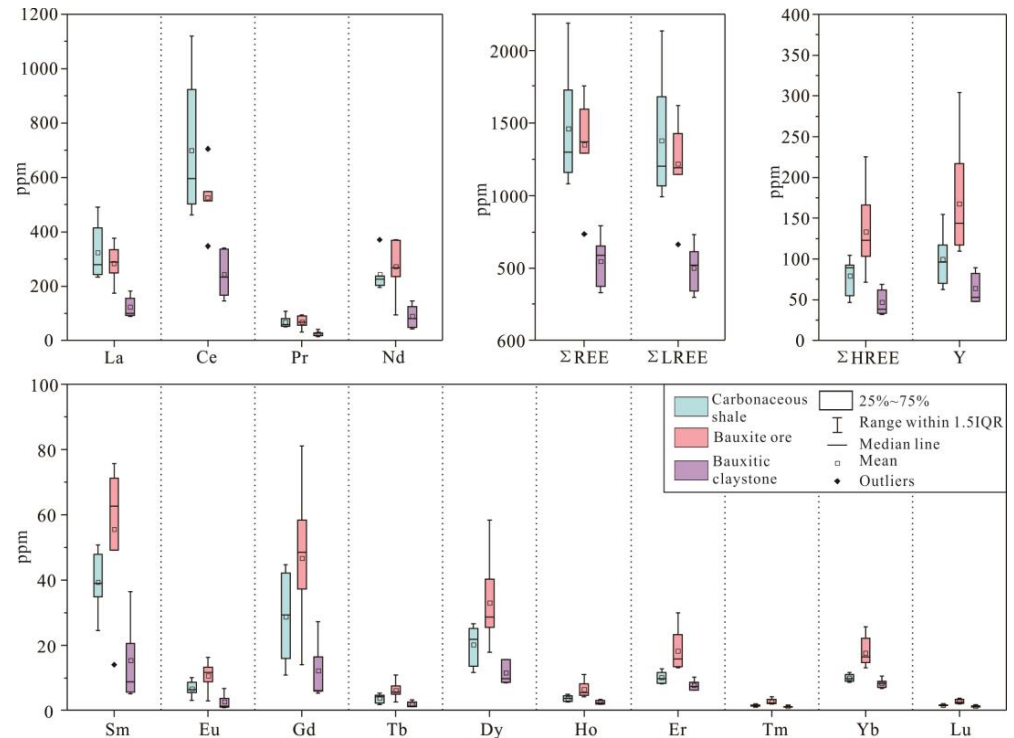


Figure 6. Boxplot of the rare earth elements contents in the bauxite ore, carbonaceous shale, and bauxitic claystone samples of the Lindai bauxite deposit (data from [28]).

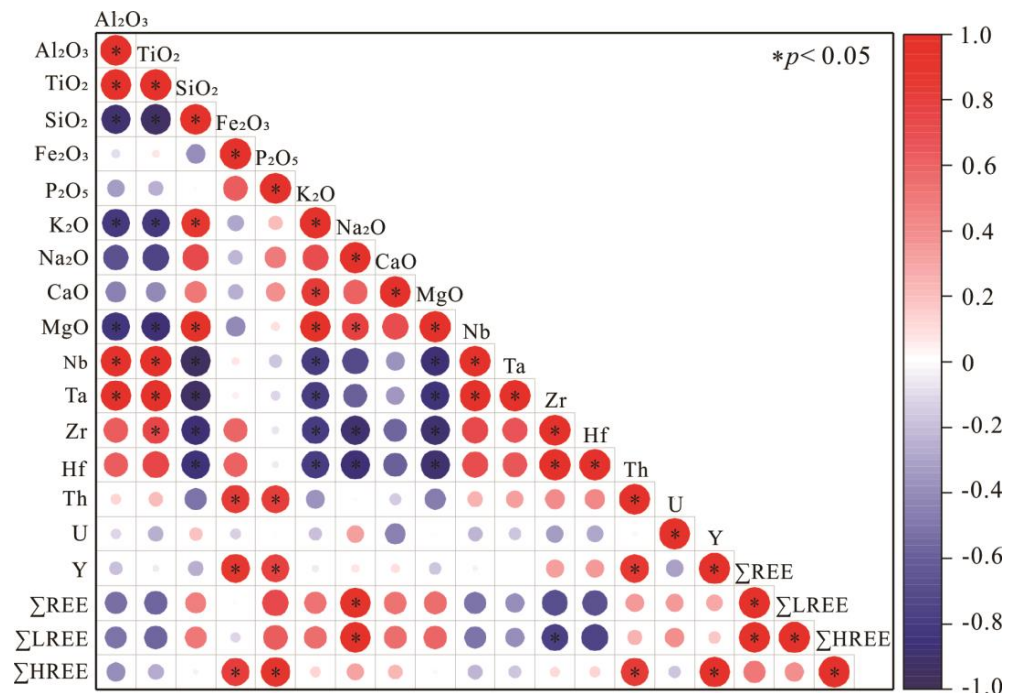


Figure 7. Correlation analyses (Pearson’s r) for selected major, trace, and rare earth elements in the Lindai bauxite deposit, central Guizhou Province (data from [28]).

4.3. REE Minerals

A relatively large number of REE minerals, including monazite and xenotime, were discovered in the bauxite ores by TIMA mineral scanning (Figure 8) and SEM-EDS observations (Figures 9 and 10). These REE-bearing mineral phases are identified as rare earth phosphate minerals and can be divided into four major groups based on their chemical composition and morphology, namely detrital monazite (Figure 9a–e), authigenic monazite (Figure 9f–i), detrital xenotime (Figure 10a–d), and authigenic xenotime (Figure 10e–i).

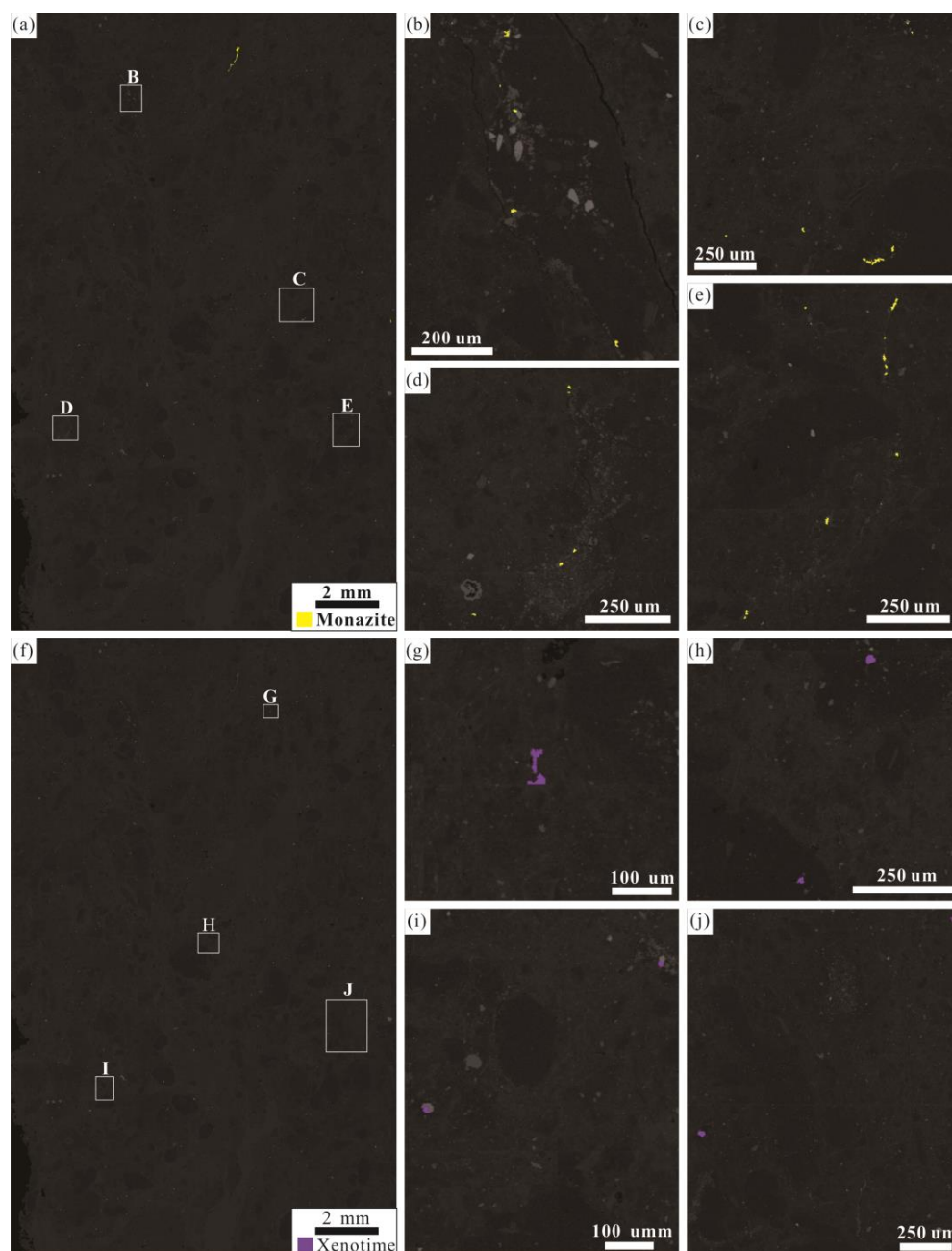


Figure 8. BSE images of monazite and xenotime from the Lindai bauxite ore obtained by TIMA mineral scanning. (a–e) Monazite and (f–j) xenotime.

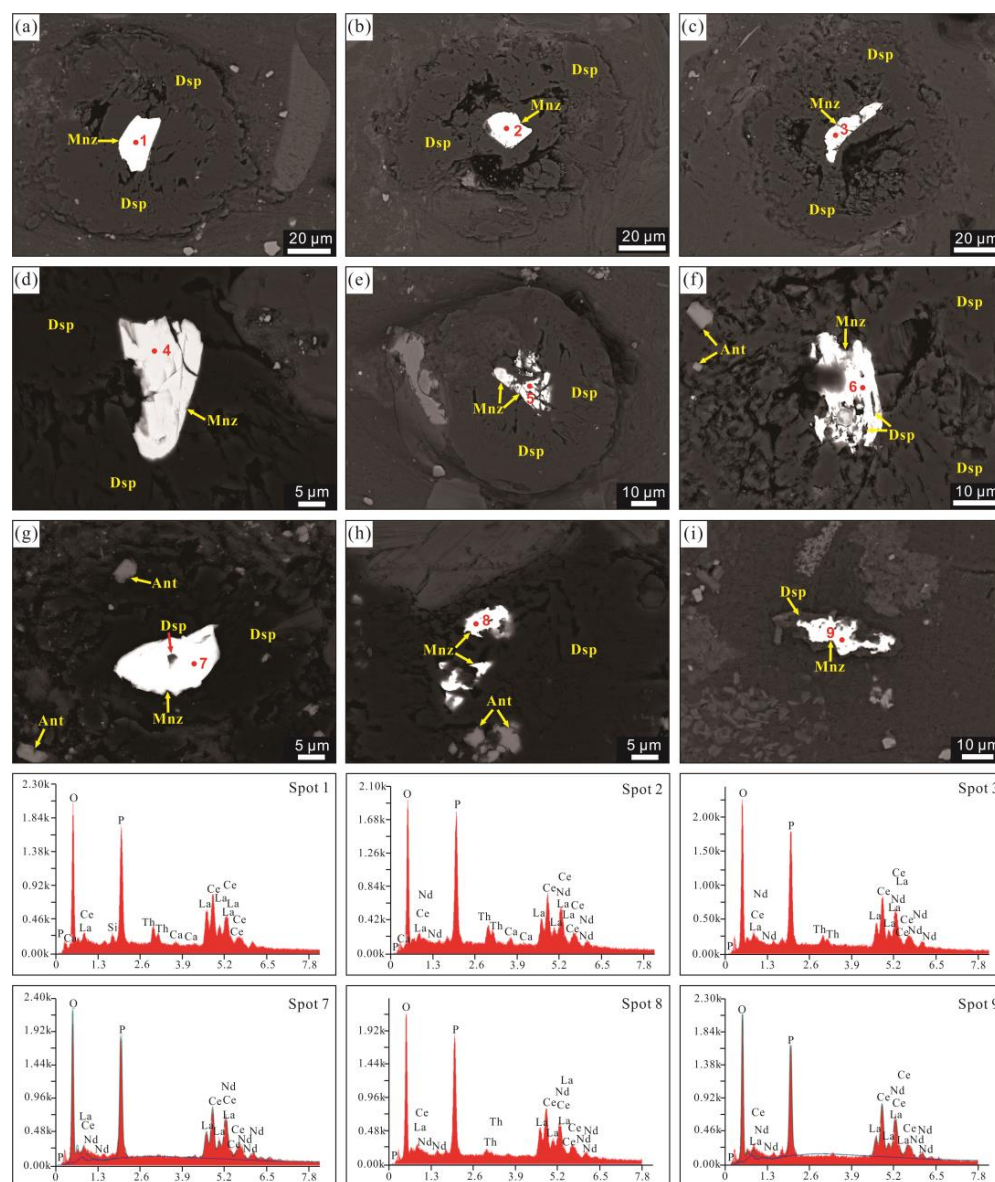


Figure 9. SEM backscattered electron (BSE) images of monazite and representative EDS spectra. (a,b) Detrital monazite presents subhedral crystals with rounded margins; (c) detrital monazite presents anhedral crystals with rounded margins; (d,e) detrital monazite presents discontinuous fragments; (f–i) authigenic monazite showing the coexistence of irregular monazite, cryptocrystalline diaspore, and euhedral anatase.

In general, detrital monazite minerals occur as subhedral (Figure 9a,b), anhedral (Figure 9c), and discontinuous fragments (Figure 9d,e) in the core of the ooid dominated by diaspore. In comparison, the authigenic monazite minerals are subhedral (Figure 9g) and have irregular shapes (Figure 9f,h,i). They commonly exhibit intergrowth with diaspore and anatase. The Th content (1.69 wt% to 5.79 wt%) is higher in the detrital monazite and is extremely low in the authigenic monazite (0 to 0.61 wt%), or no Th was detected (Table S2). Both types of monazites contain high concentrations of Nd, except for one detrital monazite. In addition, low contents of Ca and Si are observed in the detrital monazite in some cases. The EDS spectra (Figure 9) and Table S2 indicate that the detrital and authigenic monazites are enriched in LREEs, such as La, Ce, and Nd, and there are no HREEs (or they are below the detection limit of the EDS).

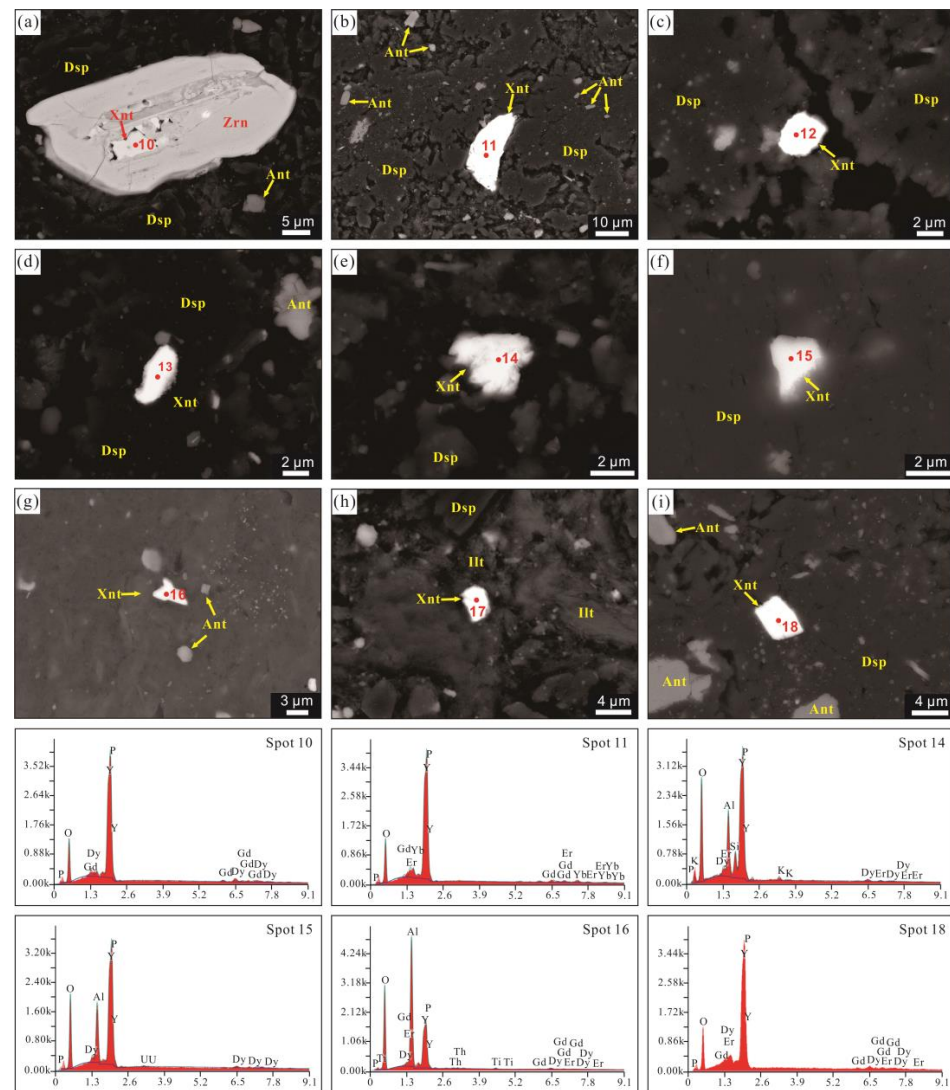


Figure 10. SEM backscattered electron (BSE) images of xenotime and representative EDS spectra. (a) Detrital xenotime showing the xenotime crystal is surrounded by zircon crystal; (b–d) detrital xenotime presents subhedral crystals with rounded margins; (e,f) authigenic xenotime presents anhedral crystals with sharp and non-round margins; (g–i) authigenic xenotime presents euhedral crystals with regular and non-round margins.

The detrital xenotime crystals are subhedral (Figure 10b–d), occurring as single crystals distributed in the matrices dominated by diaspore and illite or surrounded by zircon crystals (Figure 10a). However, the authigenic xenotime minerals are characterized by small anhedral (Figure 10e,f) and euhedral crystals (Figure 10g–i). In contrast to the monazite, the authigenic and detrital xenotimes generally contain, besides Y, substantial amounts of HREEs, such as Gd, Dy, Er, and Yb, but no LREEs (or they are below the detection limit of the EDS). Low Th and U contents are only sporadically detected in xenotime (Table S2). The occurrence of minor amounts of major elements, including Si, Al, Ti, and K, in the authigenic and detrital xenotimes can be explained by the admixture of the surrounding bauxite minerals, such as diaspore, illite, and anatase, during the composition analysis (Figure 10 and Table S2), since the xenotime grains are smaller than the diameter of the electron beam.

4.4. Genesis of REE Minerals

Monazite and xenotime, with a generalized chemical formula of [(REE) PO₄], belong to anhydrous rare-earth phosphate minerals [36]. Numerous studies have indicated that monazite and xenotime are relatively stable, weather-resistant minerals. They generally coexist within peraluminous granite, syenite, pegmatitic granite, quartz vein, carbonatite, charnockite, migmatite, and paragneiss as accessory phases, in addition to placer deposits, or are associated with coastal sediments [37–41]. In recent years, large amounts of monazite and xenotime with detrital and authigenic origins have been reported in karst bauxite deposits worldwide [3,13,21,42–46]. According to the mineralogical analysis and previous studies, the genesis of monazite and xenotime discovered in this study is discussed below.

4.4.1. Monazite

In the backscattered electron images, the monazite discovered in this study is predominantly present in two forms: surrounded by the diaspore ooid (Figure 9a–c,e) and coexisting with the cryptocrystalline diaspore aggregates and euhedral anatase (Figure 9f–i). The monazite crystals surrounded by the diaspore ooid are mainly characterized by subhedral, anhedral, and broken crystal forms. The grains are oval, elongated, approximately 20 μm in size, and have rounded margins, indicating the transportation, physical abrasion, and chemical weathering before the formation of the diaspore ooid; thus, they have a detrital origin [40]. In general, the Th content is significantly higher in monazite with a magmatic origin than that with metamorphic and sedimentary origins [47,48]. Interestingly, this pattern is also consistent with the Th content in the monazite discovered in this study, i.e., the Th content is much higher in the detrital monazite than in the authigenic monazite (Table S2). This evidence demonstrates that these monazite crystals surrounded by the diaspore ooids (Figure 9a–c,e) were inherited from the Lindai bauxite protolith (i.e., the Cambrian Shilengshui Formation dolomite, hydromica claystone, and purple-red mudstone) and were not formed during weathering and bauxitization.

In contrast, the rest of the monazite grains are characterized by subhedral, irregular shapes, commonly intergrown with the cryptocrystalline diaspore aggregates and euhedral anatase (Figure 9f–i), indicating that these monazites have co-precipitated and co-crystallized with the diaspore and anatase during ore formation. An increasing number of studies have shown that, in addition to the transformation of gibbsite and boehmite to diaspore by metamorphism, supergene crystallization under reducing and alkaline conditions is the dominant type of genesis of some diaspore and anatase in karst bauxites worldwide [8,49–52], including the Carboniferous bauxite in central Guizhou [28,53]. During the formation of the Lindai bauxite, the weathering of the parent rock consisting of dolomite, hydromica claystone, and purple-red mudstone leads to the decomposition of some primary minerals (e.g., feldspar and mica) and the formation of secondary phases such as clay minerals, as well as iron and manganese and aluminum oxides/oxyhydroxides, resulting in the adsorption of REE³⁺ released from the weathered mineral onto the surface of clay minerals [42,54–56]. Subsequently, these weathered materials (i.e., primary bauxitic materials) enriched in REE³⁺ (especially LREE³⁺) were transported by the tides (waves) generated by transgression and storm-generated seasonal floods into adjacent karstic depressions [28]. After the decomposition and transformation of minerals in the primary bauxitic materials, these REE³⁺ were released into solution [5]. The waters in the karstic depressions located above the carbonate rock are weakly alkaline to alkaline in pH [42,43,49]. Eventually, these LREE³⁺ (e.g., La, Ce, and Nd) were typically combined with phosphoric acid dissolved from the phosphate, forming authigenic monazite ((Ce, La, or Nd) PO₄), cryptocrystalline diaspore, and euhedral anatase by supergene crystallization under alkaline and reducing conditions. In contrast, the residual monazite grains formed an oolitic texture surrounded by the cryptocrystalline diaspore.

4.4.2. Xenotime

Similar to the monazite, the xenotime discovered in this study also shows evidence of detrital and authigenic origins. The detrital xenotime grains are mainly characterized by subhedral crystals (Figure 10b–d), oval grains, rounded grain margins, and a diameter of 2 to 4 μm , occasionally reaching 20 μm , indicating that these xenotime grains, similar to the monazite, originated from the Lindai bauxite protolith and experienced physical abrasion and chemical weathering during transportation and deposition. One xenotime crystal occurred as an inclusion within a single zircon crystal (Figure 10a), suggesting that both originated from the Lindai bauxite protolith. The rest of the xenotime grains have anhedral (Figure 10e,f) and euhedral crystal forms with sharp and regular margins (Figure 10g–i), suggesting an authigenic origin [57].

Previous studies have suggested that the authigenic xenotime precipitated under acidic and reducing conditions during the diagenetic stage, accompanied by sufficient concentrations of REEs, Y, and phosphate [58,59]. However, the acidic and oxidizing environments during weathering and laterization [5], as well as alkaline and reducing environments during the crystallization of monazite, diaspore, and anatase, are not suitable for the precipitation of xenotime. Therefore, the authigenic xenotime was more likely formed in the reformation stage of primary bauxitic materials with Al enrichment and Si and Fe removal after sedimentation. The acidic and reducing environments during this stage have been confirmed [25].

4.5. Occurrence Forms of REE

The REE minerals identified in this study show that the detrital and authigenic monazite are enriched with LREEs, whereas the detrital and authigenic xenotime are generally enriched with HREEs. Previous studies have shown that REEs can occur in different mineral phases in different forms, including REE individual minerals, zircon, apatite, garnet, clay minerals, Ti-bearing minerals (e.g., sphene, titanite, and rutile), and Fe and Mn oxides/hydroxides [45,60]. Therefore, in this section, the REE scanning maps obtained by TIMA analysis (Figures 11 and 12) and the correlation coefficients between the contents of REEs and some major and trace elements (Table 1) were used to identify the forms of REEs in the Lindai bauxite.

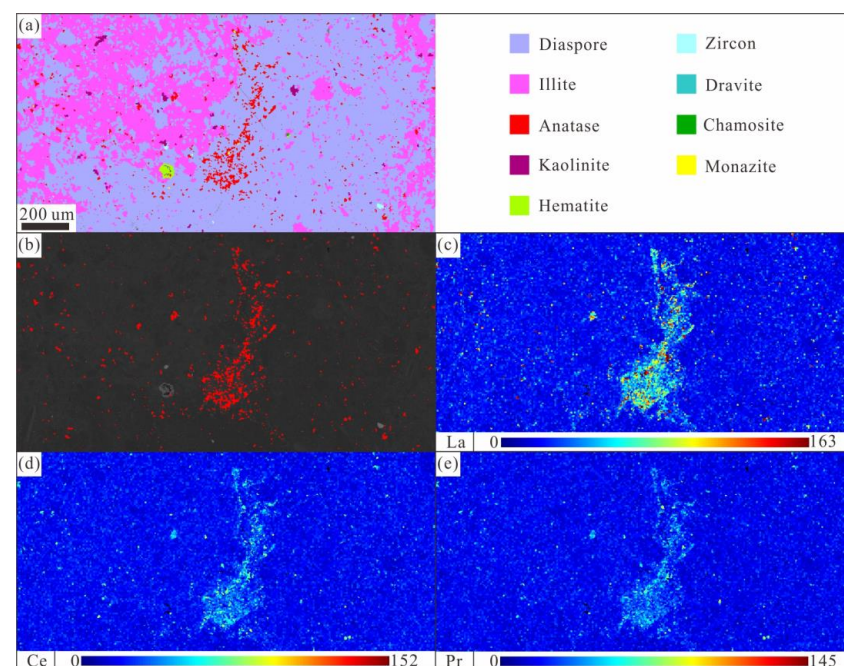


Figure 11. TIMA mineral and REE scanning maps of the representative Lindai bauxite ores. (a) All minerals; (b) anatase; (c) La element; (d) Ce element; (e) Pr element.

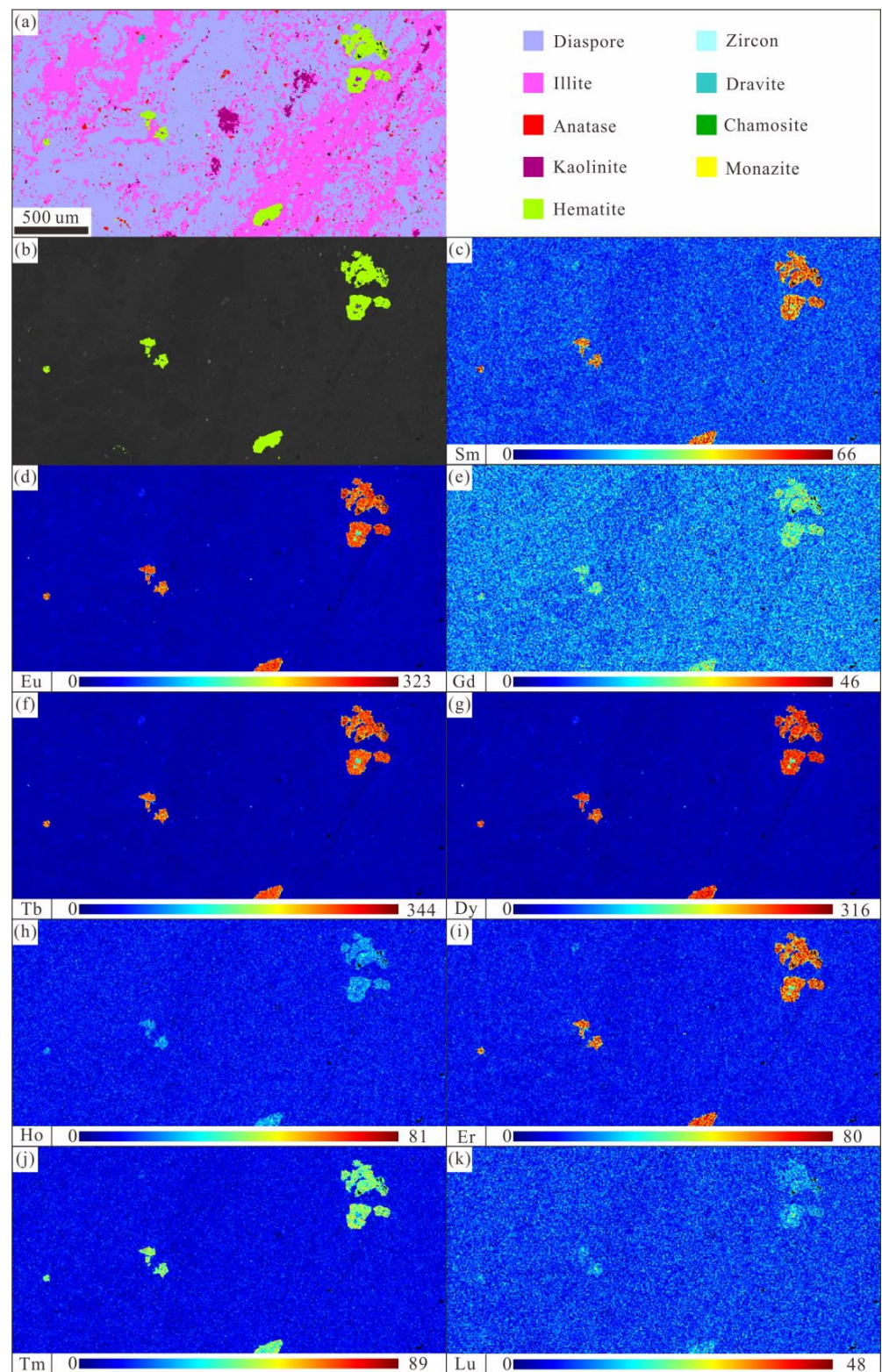


Figure 12. TIMA mineral and REE scanning maps of the representative Lindai bauxite ores. (a) All minerals; (b) hematite; (c) Sm element; (d) Eu element; (e) Gd element; (f) Tb element; (g) Dy element; (h) Ho element; (i) Er element; (j) Tm element; (k) Lu element.

Table 1. Correlation coefficients (Pearson's *r*) between REEs and some major and trace elements and REEs in the Lindai bauxite deposit, central Guizhou Province.

	SiO ₂	Al ₂ O ₃	TiO ₂	Fe ₂ O ₃	Na ₂ O	K ₂ O	CaO	MgO	MnO	P ₂ O ₅	Zr	Y
La	−0.41	0.44	0.41	−0.05	0.05	0.02	−0.39	0.39	−0.23	0.73 *	−0.09	0.39
Ce	−0.45	0.44	0.43	0.08	0.02	0.01	−0.33	−0.41	−0.09	0.83 **	−0.02	0.46
Pr	−0.25	0.29	0.25	−0.12	0.24	0.13	−0.20	−0.19	−0.27	0.70 *	−0.27	0.36
Nd	−0.19	0.21	0.16	−0.05	0.32	0.16	−0.08	−0.10	−0.19	0.74 *	−0.31	0.42
Sm	−0.22	0.09	0.06	0.43	0.25	0.05	0.07	−0.08	0.32	0.89 **	−0.08	0.74 *
Eu	−0.29	0.12	0.11	0.57	0.16	−0.01	0.02	−0.15	0.46	0.92 **	0.05	0.83 **
Gd	−0.34	0.14	0.15	0.69 *	0.06	−0.07	−0.04	−0.23	0.59	0.92 **	0.18	0.90 **
Tb	−0.43	0.22	0.25	0.75 *	−0.04	−0.16	−0.16	−0.34	0.63	0.93 **	0.30	0.95 **
Dy	−0.50	0.28	0.32	0.79 *	−0.13	−0.20	−0.24	−0.43	0.66	0.92 **	0.39	0.98 **
Ho	−0.54	0.32	0.38	0.78 *	−0.19	−0.22	−0.27	−0.47	0.65	0.89 **	0.45	0.99 **
Er	−0.58	0.38	0.44	0.76 *	−0.25	−0.25	−0.31	−0.52	0.62	0.88 **	0.49	0.99 **
Tm	−0.65	0.46	0.52	0.72 *	−0.31	−0.30	−0.37	−0.59	0.57	0.87 **	0.53	0.98 **
Yb	−0.68 *	0.51	0.57	0.67	−0.33	−0.31	−0.41	−0.62	0.50	0.86 **	0.53	0.96 **
Lu	−0.70 *	0.54	0.59	0.64	−0.34	−0.35	−0.41	−0.64	0.48	0.84 **	0.54	0.95 **

Note: * represents a significant correlation at $p < 0.05$ and ** represents a highly significant correlation at $p < 0.01$.

A correlation analysis of REEs and major and trace elements showed that the REE content has no or weak correlation with the Al₂O₃, SiO₂, K₂O, Na₂O, CaO, MgO, and Zr contents, indicating that Al oxyhydroxides (e.g., diaspore and boehmite), clay minerals (e.g., kaolinite and illite), and zircon have a negligible impact on the REE distribution [3]. However, the Sm, Eu, and HREE contents have a moderate to significantly positive correlation ($R^2 = 0.43 - 0.79$) with the Fe₂O₃ content, which seems to indicate that Fe oxides/hydroxides (e.g., hematite and goethite) have an important role in the enrichment of HREEs, in addition to xenotime [61,62]. In addition, the REE content has significantly positive correlations with the P₂O₅ and Y contents, suggesting that the REE distributions were also associated with Y- and P-bearing REE minerals [62]. Thus, the correlation analysis results indicate that we cannot exclude the possibility that Fe oxides/hydroxides control the distribution of some HREEs.

On the other hand, the REE (La–Lu) scanning maps obtained by the TIMA analysis show that, in addition to the anatase and hematite, no REE distribution was found in other rock-forming minerals including diaspore, illite, kaolinite, and zircon (Figures 11 and 12). Combined with the correlation analysis, this further confirms that diaspore, clay minerals, and zircon are not the host minerals of REEs in the bauxite ore. In contrast, some LREEs, including La, Ce, and Pr, are enriched in the anatase in addition to the monazite (Figure 11a–e), whereas the hematite also controls relatively large amounts of Sm, Eu, and HREE (such as Gd, Tb, Dy, Ho, Er, Tm, and Lu) distributions (Figure 12a–k). Although many scholars have recognized that Fe oxides/hydroxides and Ti-bearing minerals have important roles in the REE distribution and act as scavengers for REEs [8,63,64], the mechanism of REE scavenging by hematite and anatase are not well understood [62]. Of course, we cannot yet comment on the mechanism of REE scavenging by hematite and anatase at this stage, but this will be an interesting direction for future studies.

In summary, REEs in the Lindai bauxite deposit exhibit multiple forms, including the rare-earth phosphate minerals (monazite and xenotime) and REE scavenging by hematite and anatase phases. Based on the percentage composition of REE-bearing mineral phases, including monazite, xenotime, hematite, and anatase, in the bauxite ore, the percentage of each occurrence form was calculated. Namely, the REE scavenging by hematite accounted for 93.28% of all forms of REEs, REE scavenging by anatase accounted for 5.88%, monazite accounted for 0.67%, and xenotime accounted for 0.17%.

4.6. Implications for the Formation of Bauxite

Although previous studies have demonstrated that the bauxite deposits in central Guizhou are mainly derived from the underlying Cambrian dolomite [25], Luo et al. [28]

believed that at least the source rock of the Lindai bauxite in the Qingzhen area was dominated by aluminosilicate rock based on a geochemical investigation. After all, the aluminum contents of hydromica claystone (24.96% to 25.60%) and purple-red mudstone (8.33% to 10.40%) in the Cambrian Shilengshui Formation are approximately 26.9- and 10-fold higher than those in the dolomite (0.26% and 1.61%, respectively) [28]. Generally, the vast majority of REEs in the sedimentary rock are considered to be enriched in detrital clay and silt particles, as well as in heavy mineral phases, such as zircon, rutile, and monazite [59]. It is indisputable that REEs and REE-bearing minerals in carbonate rock are extremely rare. Therefore, the presence of large numbers of weather-resistant minerals, including detrital monazite and xenotime, in the bauxite ores suggests the contribution of aluminosilicate rock to the formation of the Lindai bauxite. Most of these weather-resistant minerals originate from the parent rock of the bauxite, suggesting that the bauxite deposits, whose underlying and surrounding strata are dominated by aluminosilicate rock, are the most likely source of the REEs.

Although the Carboniferous karst bauxite deposits in central Guizhou are thought to have formed during the early middle stage of the Mississippian Visean age, there has been a lack of reliable isotope chronological evidence to determine the formation age. Interestingly, the identification of authigenic monazite and xenotime minerals enables us to use Th–U–Pb isotope chronology to determine the formation age of karst bauxite in central Guizhou Province. Certainly, this possibility will be investigated in-depth in a follow-up study.

5. Conclusions

(1) The mineralogical evidence obtained by TIMA analysis and SEM-EDS observations shows that the forms of REEs in the Lindai bauxite deposit include rare-earth phosphate minerals (monazite and xenotime) and REE scavenging by hematite and anatase phases.

(2) REE (La–Lu) scanning maps obtained by TIMA analysis show that, in addition to the hematite and anatase, no REE distribution was found in the diaspore, illite, kaolinite, and zircon. Among them, the anatase controls some LREE (such as La, Ce, and Pr) distributions, whereas the hematite also controls relatively large amounts of Sm, Eu, and HREE (such as Gd, Tb, Dy, Ho, Er, Tm, and Lu) distributions.

(3) Based on the percentage composition of REE-bearing mineral phases, REE scavenging by hematite accounted for 93.28%, REE scavenging by anatase accounted for 5.88%, monazite accounted for 0.67%, and xenotime accounted for 0.17% of all forms of REEs.

Supplementary Materials: The following supporting information can be downloaded at: <https://www.mdpi.com/article/10.3390/min13030320/s1>, Table S1: The rare earth elements contents (ppm) of the Jiujiayu Formation ore-bearing rock series from the Lindai bauxite deposit, central Guizhou Province [65]; Table S2: EDS microanalyses of the monazite and xenotime in the Lindai bauxite deposit, central Guizhou Province.

Author Contributions: Conceptualization, C.L. and R.Y.; methodology, C.L. and R.Y.; software, P.L. and Q.C.; validation, J.G.; investigation, C.L. and P.L.; resources, R.Y. and Q.C.; data curation, H.M.; writing—original draft preparation, C.L. and P.L.; writing—review and editing, C.L. and Q.C.; visualization, J.G. and H.M.; supervision, R.Y.; project administration, R.Y.; funding acquisition, R.Y. and Q.C. All authors have read and agreed to the published version of the manuscript.

Funding: This work was financially supported by the Project of Research, Development and Application of Key Technologies for Big Data Prediction of Bauxite Resources in Guizhou Province (No. [2022]ZD003-3), the National Natural Science Foundation of China (No. U1812402), the Project of Scientific and Technological Innovation Team of Sedimentary Deposits in Guizhou Province (No. 2018-5613), the Project of Graduate Scientific Research Fund of Guizhou Province (No. YJSKYJJ [2021]075), and the Contract Number: Qian Dikuang Kehe [2021]No. 5.

Data Availability Statement: Not applicable.

Acknowledgments: We are grateful to editor and three anonymous reviewers for their critical reviews and numerous suggestions for improvement of this manuscript.

Conflicts of Interest: The authors declare no conflict of interest.

References

1. European Commission. Study on the EU's list of Critical Raw Materials—Final Report. 2020. Available online: <https://ec.europa.eu/docsroom/documents/42883/attachments/1/translations/en/renditions/native> (accessed on 5 June 2020).
2. Linnen, R.L.; Samson, I.M.; Williams-Jones, A.E.; Chakhmouradian, A.R. Geochemistry of the rare-earth elements, Nb, Ta, Hf and Zr deposits. In *Treatise on Geochemistry*, 2nd ed.; Turekian, K.K., Ed.; Elsevier: Amsterdam, The Netherlands, 2014; pp. 543–568.
3. Reinhardt, N.; Proenza, J.A.; Villanova-de-Benavent, C.; Aiglsperger, T.; Bover-Arnal, T.; Torró, L.; Salas, R.; Dziggel, A. Geochemistry and Mineralogy of Rare Earth Elements (REE) in Bauxitic Ores of the Catalan Coastal Range, NE Spain. *Minerals* **2018**, *8*, 562–586. [[CrossRef](#)]
4. Voncken, J.H.L. The ore minerals and major ore deposits of the rare earths. In *The Rare Earth Elements*; Voncken, J.H.L., Ed.; Springer: Cham, Switzerland, 2016; pp. 15–52.
5. Liu, X.F.; Wang, Q.F.; Zhang, Q.Z.; Zhang, Y.; Li, Y. Genesis of REE minerals in the karstic bauxite in western Guangxi, China, and its constraints on the deposit formation conditions. *Ore Geol. Rev.* **2016**, *75*, 100–115. [[CrossRef](#)]
6. Kiaeshkevarian, M.; Calagari, A.A.; Abedini, A.; Shamanian, G. Geochemical and mineralogical features of karst bauxite deposits from the Alborz zone (Northern Iran): Implications for conditions of formation, behavior of trace and rare earth elements and parental affinity. *Ore Geol. Rev.* **2016**, *125*, 103691. [[CrossRef](#)]
7. Abedini, A.; Khosravi, M.; Dill, H.G. Rare earth element geochemical characteristics of the late Permian Badamlu karst bauxite deposit, NW Iran. *J. Afr. Earth Sci.* **2020**, *172*, 103974. [[CrossRef](#)]
8. Ahmadnejad, F.; Zamanian, H.; Taghipour, B.; Zarasvandi, A.; Buccione, R.; Ellahi, S.S. Mineralogical and geochemical evolution of the Bidgol bauxite deposit, Zagros Mountain Belt, Iran: Implications for ore genesis, rare earth elements fractionation and parental affinity. *Ore Geol. Rev.* **2017**, *86*, 755–783. [[CrossRef](#)]
9. Long, Y.Z.; Chi, G.X.; Liu, J.P.; Jin, Z.G.; Dai, T.G. Trace and rare earth elements constraints on the sources of the Yunfeng paleo-karstic bauxite deposit in the Xiuwen-Qingzhen area, Guizhou, China. *Ore Geol. Rev.* **2017**, *91*, 404–418. [[CrossRef](#)]
10. Abedini, A.; Mongelli, G.; Khosravi, M.; Sinisi, R. Geochemistry and secular trends in the middle–late Permian karst bauxite deposits, northwestern Iran. *Ore Geol. Rev.* **2020**, *124*, 103660. [[CrossRef](#)]
11. Abedini, A.; Mongelli, G.; Khosravi, M. Geochemistry of the early Jurassic Soleiman Kandi karst bauxite deposit, Irano–Himalayan belt, NW Iran: Constraints on bauxite genesis and the distribution of critical raw materials. *J. Geochem. Explor.* **2022**, *241*, 107056. [[CrossRef](#)]
12. Abedini, A.; Khosravi, M.; Calagari, A.A. Geochemical characteristics of the Arbanos karst-type bauxite deposit, NW Iran: Implications for parental affinity and factors controlling the distribution of elements. *J. Geochem. Explor.* **2019**, *200*, 249–265. [[CrossRef](#)]
13. Abedini, A.; Mongelli, G.; Khosravi, M. Geochemical constraints on the middle Triassic Kani Zarrineh karst bauxite deposit, Irano–Himalayan belt, NW Iran: Implications for elemental fractionation and parental affinity. *Ore Geol. Rev.* **2021**, *133*, 104099. [[CrossRef](#)]
14. Gao, L.; Li, J.H.; Wang, D.H.; Xiong, X.Y.; Yi, C.W.; Han, M.Z. Outline of Metallogenic Regularity of Bauxite Deposits in China. *Acta Geol. Sin.* **2015**, *89*, 2072–2084.
15. Wang, Q.F.; Deng, J.; Liu, X.F.; Zhang, Q.Z.; Sun, S.L.; Jiang, C.Z.; Zhou, F. Discovery of the REE minerals and its geological significance in the Quyang bauxite deposit, West Guangxi, China. *J. Asian Earth Sci.* **2010**, *39*, 701–712. [[CrossRef](#)]
16. Deady, E.A.; Mouchos, E.; Goodenough, K.; Williamson, B.J.; Wall, F. A review of the potential for rare-earth element resources from European red muds: Examples from Seydişehir, Turkey and Parnassus-Giona, Greece. *Mineral. Mag.* **2016**, *80*, 43–61. [[CrossRef](#)]
17. Gamaletsos, P.N.; Godelitsas, A.; Filippidis, A.; Pontikes, Y. The rare Earth elements potential of Greek Bauxite active Mines in the Light of a Sustainable REE demand. *J. Sustain. Metall.* **2018**, *5*, 20–47. [[CrossRef](#)]
18. Horbe, A.M.C.; Costa, M.L.D. Geochemical evolution of a lateritic Sn Zr Th Nb Y REE-bearing ore body derived from apogranite: The case of Pitinga, Amazonas-Brazil. *J. Geochem. Explor.* **1999**, *66*, 339–351. [[CrossRef](#)]
19. Li, Z.H.; Din, J.; Xu, J.S.; Liao, C.G.; Yin, F.G.; Lu, T.; Cheng, L.; Li, J.M. Discovery of the REE minerals in the Wulong–Nanchuan bauxite deposits, Chongqing, China: Insights on conditions of formation and processes. *J. Geochem. Explor.* **2013**, *133*, 88–102. [[CrossRef](#)]
20. Wang, X.M.; Jiao, Y.Q.; Du, Y.S.; Ling, W.L.; Wu, L.Q.; Cui, T.; Zhou, Q.; Jin, Z.G.; Lei, Z.Y.; Weng, S.F. REE mobility and Ce anomaly in bauxite deposit of WZD area, Northern Guizhou, China. *J. Geochem. Explor.* **2013**, *133*, 103–117. [[CrossRef](#)]
21. Zhu, K.Y.; Su, H.M.; Jiang, S.Y. Mineralogical control and characteristics of rare earth elements occurrence in Carboniferous bauxites from western Henan Province, north China: A XRD, SEM-EDS and LA-ICP-MS analysis. *Ore Geol. Rev.* **2019**, *114*, 10314. [[CrossRef](#)]
22. Sun, L.; Xiao, K.Y.; Lou, D.B. Mineral prospectivity of bauxite resources in China. *Earth Sci. Front.* **2018**, *25*, 82–94. (In Chinese)
23. Gao, D.D.; Sheng, Z.Q.; Shi, S.H.; Chen, L.A. *Studies on the Bauxite Deposit in Central Guizhou*; Guizhou Science and Technology Publishing House: Guiyang, China, 1992; pp. 1–152. (In Chinese)
24. Ling, K.Y.; Zhu, X.Q.; Tang, H.S.; Wang, Z.G.; Yan, H.W.; Han, T.; Chen, W.Y. Mineralogical characteristics of the karstic bauxite deposits in the Xiuwen ore belt, Central Guizhou Province, Southwest China. *Ore Geol. Rev.* **2015**, *65*, 84–96. [[CrossRef](#)]

25. Ling, K.Y.; Zhu, X.Q.; Tang, H.S.; Li, S.X. Importance of hydrogeological conditions during formation of the karstic bauxite deposits, Central Guizhou Province, Southwest China: A case study at Lindai deposit. *Ore Geol. Rev.* **2017**, *82*, 198–216. [[CrossRef](#)]
26. Wang, R.X.; Wang, Q.F.; Huang, Y.X.; Yang, S.J.; Liu, X.F.; Zhou, Q. Combined tectonic and paleogeographic controls on the genesis of bauxite in the Early Carboniferous to Permian Central Yangtze Island. *Ore Geol. Rev.* **2018**, *101*, 468–480. [[CrossRef](#)]
27. Yang, R.D.; Gao, J.B.; Zhao, K.; Yu, J.L.; Zhu, C.L.; Gao, L.; Chen, J.Y.; Zhou, R.X. Roof and Floor Characteristics of Bauxite in Qingzhen, Guizhou and Its Implication for Bauxite Mineralization. *Acta Geol. Sinica* **2018**, *92*, 2155–2165, (in Chinese with English abstract).
28. Luo, C.K.; Yang, R.D.; Chen, J.; Gao, L.; Xu, H.; Ni, X.R. Genesis of the Carboniferous karstic bauxites in Qingzhen region, central Guizhou, southwest China. *J. Geochem. Explor.* **2022**, *235*, 106955. [[CrossRef](#)]
29. Wu, L.; Huang, Z.L.; Wang, Z.L.; Wang, Y.F.; Chen, J.; Wu, T. Geochemistry of bauxite in the Maochang deposit, central Guizhou. *Acta Mineral. Sin.* **2021**, *41*, 475–484. (In Chinese)
30. Liu, W.; Xu, X.S.; Yu, Q. Discussion on Forming Mechanism and Evolution of the Central Guizhou Palaeouplift. *Acta Sedimentol. Sin.* **2011**, *29*, 658–664. (In Chinese with English abstract).
31. Deng, X.; Yang, K.G.; Liu, Y.L.; She, Z.B. Characteristics and tectonic evolution of Qianzhong Uplift. *Earth Science Frontiers* **2010**, *17*, 79–89. (In Chinese with English abstract).
32. Liu, P.; Liao, Y.C. A tentative discussion on the age of bauxite-bearing rock series in Central Guizhou-Southern Chongqing area. *Geol. China* **2012**, *39*, 661–682, (In Chinese with English abstract).
33. Guizhou Geological Survey Institute. *Regional Geology of China: Geological Marks of Guizhou Province*; Geological Publishing House: Beijing, China, 2017. (In Chinese)
34. Luo, C.K.; Yang, R.D.; Gao, J.B.; Umair, M.; Wang, L.B.; Gao, L. Viséan Fossil Plants from the Jiujialu Formation in Central Guizhou Province: Implications for Age of Bauxite and Palaeoenvironment. *Acta Geol. Sin.* **2020**, *94*, 2165–2177. [[CrossRef](#)]
35. Yin, Z.M. The Texture and Structure features of Carboniferous Bauxite in China and Its Emplacement Mechanism. *J. Cent. South Univ. Min. Metall.* **1988**, *19*, 357–363.
36. Clavier, N.; Mesbah, A.; Szenknect, S.; Dacheux, N. Monazite, rhabdophane, xenotime & churchite: Vibrational spectroscopy of gadolinium phosphate polymorphs. *Spectrochim. Acta Part A Mol. Biomol. Spectrosc.* **2018**, *205*, 85–94.
37. Rapp, R.P.; Watson, E.B. Monazite solubility and dissolution kinetics: Implications for the thorium and light rare earth chemistry of felsic magmas. *Contrib. Mineral. Petrol.* **1986**, *94*, 304–316. [[CrossRef](#)]
38. Forster, H.J. The chemical composition of REE-Y-Th-U-rich accessory minerals in peraluminous granites of the Erzgebirge-Fichtelgebirge region, Germany. Part II: Xenotime. *Am. Mineral.* **1998**, *83*, 1302–1315. [[CrossRef](#)]
39. Williams, M.L.; Jercinovic, M.J.; Hetherington, C.J. Microprobe monazite geochronology: Understanding geologic processes by integrating composition and chronology. *Annu. Rev. Earth Planet. Sci.* **2007**, *35*, 137–175. [[CrossRef](#)]
40. Santana, I.V.; Wall, F.; Botelho, N.F. Occurrence and behavior of monazite-(Ce) and xenotime-(Y) in detrital and saprolitic environments related to the Serra Dourada granite, Goiás/Tocantins State, Brazil: Potential for REE deposits. *J. Geochem. Explor.* **2015**, *155*, 1–13. [[CrossRef](#)]
41. Xu, H.; Gao, J.B.; Yang, R.D.; Du, L.J.; Liu, Z.C.; Chen, J.; Feng, K.N.; Yang, G.H. Genesis for Rare Earth Elements Enrichment in the Permian Manganese Deposits in Zunyi, Guizhou Province, SW China. *Acta Geol. Sin.* **2020**, *94*, 90–102. [[CrossRef](#)]
42. Maksimović, Z.; Pantó, G. Contribution to the geochemistry of the rare earth elements in the karst-bauxite deposits of Yugoslavia and Greece. *Geoderma* **1991**, *51*, 93–109. [[CrossRef](#)]
43. Mongelli, G. Ce-anomalies in the textural components of Upper Cretaceous karst bauxites from the Apulian carbonate platform (southern Italy). *Chem. Geol.* **1997**, *140*, 69–79. [[CrossRef](#)]
44. Mondillo, N.; Balassone, G.; Boni, M.; Rollinson, G. Karst bauxites in the Campania Apennines (southern Italy): A new approach. *Period. Mineral.* **2011**, *80*, 407–432.
45. Radusinović, S.; Jelenković, R.; Pačevski, A.; Simić, V.; Božović, D.; Holclajtner-Antunović, I.; Životić, D. Content and mode of occurrences of rare earth elements in the Zagrad karstic bauxite deposit (Nikšić area, Montenegro). *Ore Geol. Rev.* **2017**, *80*, 406–428. [[CrossRef](#)]
46. Rudmin, M.; Reva, I.; Sokol, E.; Abdullayev, E.; Ruban, A.; Kudryavtsev, A.; Tolkachev, O.; Mazurov, A. Minerals of Rare Earth Elements in High-Phosphorus Ooidal Ironstones of the Western Siberia and Turgai Depression. *Minerals* **2020**, *10*, 11. [[CrossRef](#)]
47. Schandl, E.S.; Gorton, M.P. A textural and geochemical guide to the identification of hydrothermal monazite: Criteria for selection of samples for dating epigenetic hydrothermal ore deposits. *Econ. Geol.* **2004**, *99*, 1027–1035. [[CrossRef](#)]
48. Aleinikoff, J.N.; Slack, J.F.; Lund, K.; Evans, K.V.; Fanning, C.M.; Mazdab, F.K.; Wooden, J.L.; Pillers, R.M. Constraints on the Timing of Co-Cu±Au Mineralization in the Blackbird District, Idaho, Using SHRIMP U-Pb Ages of Monazite and Xenotime Plus Zircon Ages of Related Mesoproterozoic Orthogneisses and Metasedimentary Rocks. *Econ. Geol.* **2012**, *107*, 1143–1175. [[CrossRef](#)]
49. Liu, X.F.; Wang, Q.F.; Zhang, Q.Z.; Feng, Y.W.; Cai, S.H. Mineralogical characteristics of the superlarge Quaternary bauxite deposits in Jingxi and Debao counties, western Guangxi, China. *J. Asian Earth Sci.* **2012**, *52*, 53–62. [[CrossRef](#)]
50. Liu, X.F.; Wang, Q.F.; Feng, Y.W.; Li, Z.M.; Cai, S.H. Genesis of the Guangou karstic bauxite deposit in western Henan, China. *Ore Geol. Rev.* **2013**, *55*, 162–175. [[CrossRef](#)]
51. Yang, S.J.; Wang, Q.F.; Deng, J.; Wang, Y.Z.; Kang, W.; Liu, X.F.; Li, Z.M. Genesis of karst bauxite-bearing sequences in Baofeng, Henan (China), and the distribution of critical metals. *Ore Geol. Rev.* **2019**, *115*, 103–161. [[CrossRef](#)]

52. Zhang, L.; Park, C.Y.; Wang, G.H.; Wu, C.J.; Santosh, M.; Chung, D.H.; Song, Y.G. Phase transformation processes in karst-type bauxite deposit from Yunnan area, China. *Ore Geol. Rev.* **2017**, *89*, 407–420. [[CrossRef](#)]
53. Wang, R.X.; Wang, Q.F.; Uysal, I.T.; Ramanaidou, E.; Deng, J.; Todd, A. Mesozoic Hydrothermal Overprint on Carboniferous Bauxite in China. *Econ. Geol.* **2021**, *116*, 787–800. [[CrossRef](#)]
54. Coppin, F.; Berger, G.; Bauer, A.; Castet, S.; Loubet, M. Sorption of lanthanides on smectite and kaolinite. *Chem. Geol.* **2002**, *182*, 57–68. [[CrossRef](#)]
55. Karakaya, N. REE and HFS element behaviour in the alteration facies of the Erenler Dağı Volcanics (Konya, Turkey) and kaolinite occurrence. *J. Geochem. Explor.* **2009**, *101*, 185–208. [[CrossRef](#)]
56. Menéndez, I.; Campeny, M.; Quevedo-González, L.; Mangas, J.; Llovet, X.; Tauler, E.; Barfon, V.; Torrent, J.; Méndez-Ramos, J. Distribution of REE-bearing minerals in felsic magmatic rocks and paleosols from Gran Canaria, Spain: Intraplate oceanic islands as a new example of potential, non-conventional sources of rare-earth elements. *J. Geochem. Explor.* **2019**, *204*, 270–288. [[CrossRef](#)]
57. Lan, Z.W.; Li, X.H.; Sano, Y.; Takahata, N.; Kagoshima, T.; Zhang, S.J.; Zhang, G.Y.; Liao, X.; Tang, X.; Gu, L.X.; et al. Two kinds of authigenic xenotime overgrowths in response to an Early Paleozoic tectonothermal event in South China. *J. Asian Earth Sci.* **2018**, *172*, 423–442. [[CrossRef](#)]
58. Rasmussen, B. Early-diagenetic REE-phosphate minerals (florencite, gorceixite, crandallite, and xenotime) in marine sandstones; a major sink for oceanic phosphorus. *Am. J. Sci.* **1996**, *296*, 601–632. [[CrossRef](#)]
59. Rasmussen, B.; Buick, R.; Taylor, W.R. Removal of oceanic REE by authigenic precipitation of phosphatic minerals. *Earth Planet. Sci. Lett.* **1998**, *164*, 135–149. [[CrossRef](#)]
60. Laveuf, C.; Cornu, S. A review on the potentiality of Rare Earth Elements to trace pedogenetic processes. *Geoderma* **2009**, *154*, 1–12. [[CrossRef](#)]
61. Ohta, A.; Kawabe, I. REE(III) adsorption into Mn dioxide (a-MnO₂) and Fe oxyhydroxide: Ce (III) oxidation by a-MnO₂. *Geochim. Cosmochim. Acta* **2001**, *65*, 695–703. [[CrossRef](#)]
62. Ahmadnejad, F.; Mongelli, G. Geology, geochemistry, and genesis of REY minerals of the late Cretaceous karst bauxite deposits, Zagros Simply Folded Belt, SW Iran: Constraints on the ore-forming process. *J. Geochem. Explor.* **2022**, *240*, 107030. [[CrossRef](#)]
63. Kühnel, R.A. The Role of Cationic and Anionic Scavengers in Laterites. *Chem. Geol.* **1987**, *60*, 31–40. [[CrossRef](#)]
64. Mondillo, N.; Balassone, G.; Boni, M.; Chelle-Michou, C.; Cretella, S.; Mormone, A.; Putzolu, F.; Santoro, L.; Scognamiglio, G.; Tarallo, M. Rare Earth Elements (REE) in Al- and Fe-(Oxy)-Hydroxides in Bauxites of Provence and Languedoc (Southern France): Implications for the Potential Recovery of REEs as By-Products of Bauxite Mining. *Minerals* **2019**, *9*, 504. [[CrossRef](#)]
65. Sun, S.S.; McDonough, W.F. Chemical and isotopic systematics of oceanic basalts: Implications for mantle composition and processes. *Geol. Soc. Lond. Spec. Publ.* **1989**, *42*, 313–345.

Disclaimer/Publisher’s Note: The statements, opinions and data contained in all publications are solely those of the individual author(s) and contributor(s) and not of MDPI and/or the editor(s). MDPI and/or the editor(s) disclaim responsibility for any injury to people or property resulting from any ideas, methods, instructions or products referred to in the content.